

See discussions, stats, and author profiles for this publication at: <https://www.researchgate.net/publication/227715419>

# Optical micro-characterization of group-III-nitrides: Correlation of structural, electronic and optical properties

ARTICLE *in* PHYSICA STATUS SOLIDI (C) · SEPTEMBER 2003

DOI: 10.1002/pssc.200303125

---

CITATIONS

13

---

READS

25

9 AUTHORS, INCLUDING:



**Christian Thomsen**

Technische Universität Berlin

**591** PUBLICATIONS **15,506** CITATIONS

SEE PROFILE

## Optical micro-characterization of group-III-nitrides: correlation of structural, electronic and optical properties

J. Christen<sup>\*1</sup>, T. Riemann<sup>1</sup>, F. Bertram<sup>1</sup>, D. Rudloff<sup>1</sup>, P. Fischer<sup>1</sup>, A. Kaschner<sup>2</sup>, U. Haboeck<sup>2</sup>, A. Hoffmann<sup>2</sup>, and C. Thomsen<sup>2</sup>

<sup>1</sup> Institut für Experimentelle Physik, Otto-von-Guericke-Universität Magdeburg, Germany

<sup>2</sup> Institut für Festkörperphysik, Technische Universität Berlin, Germany

Received 4 March 2003, revised 5 May 2003, accepted 7 May 2003

Published online 28 August 2003

PACS 61.72.Ss, 78.30.Fs, 78.60.Hk

For a detailed understanding of complex semiconductor heterostructures and the physics of devices based on them, a systematic determination and correlation of the structural, chemical, electronic, and optical properties on a micro- or nano-scale is essential. Luminescence techniques belong to the most sensitive, non-destructive methods of semiconductor research. The combination of luminescence spectroscopy with the high spatial resolution of a scanning electron microscope, as realized by the technique of cathodoluminescence microscopy, provides a powerful tool for the optical nano-characterization of semiconductors, their heterostructures as well as their interfaces. Additional access to the local electronic and structural properties is provided by micro-Raman spectroscopy, e.g. giving insight into the local free carrier concentration and local stress. In this paper, the properties of group-III-nitrides are investigated by highly spatially and spectrally resolved cathodoluminescence microscopy in conjunction with micro-Raman spectroscopy. Complex phenomena of self-organization and their strong impact on the microscopic and nanoscopic properties of both binary and ternary nitrides are presented. As the ultimate measure of device performance, the microscopic properties of light emitting diodes are assessed under operation. Using micro-electroluminescence mapping in the optical microscope as well as in the near field detection mode of a scanning near field optical microscope, the microscopic origin of the macroscopic spectral red shift in light emitting diodes is identified.

© 2003 WILEY-VCH Verlag GmbH & Co. KGaA, Weinheim

### 1 Introduction

All ternary or quaternary semiconductor alloys are subject to statistical stoichiometry fluctuations on a sub-microscopic scale. This intrinsic disorder becomes in particular important when lattices mismatch and restricted solubility is involved as given for the case of group-III-nitride alloys. Spatial energy fluctuations extending from atomic scale for perfect alloys up to micrometers for phase separation have a strong impact on both the electronic and optical material properties of the nitrides and the performance of the devices fabricated from them. The situation becomes even more complex for non-homogeneous growth modes of selective local epitaxy. The crystal growth on pre-patterned substrates, as for example used in epitaxial lateral overgrowth GaN (ELOG) [1, 2], results in a complex spatial structure of self-organized micro-domains having dramatic differences in defect density [3, 4] and impurity incorporation [5–9] and, in the case of alloys, stoichiometry [10, 11].

<sup>\*</sup> Corresponding author: e-mail: juergen.christen@physik.uni-magdeburg.de,  
Phone: +49 391 67 18668, Fax: +49 391 67 11130

© 2003 WILEY-VCH Verlag GmbH & Co. KGaA, Weinheim

InGaN is the material of choice for opto-electronic devices operating in the near ultraviolet (UV), blue, and green spectral range [12, 13]. However, the ternary alloy InGaN is known to be a strongly inhomogeneous system [14] with local variation of the In-concentration [15], and strain, i.e. local band-gap [16]. While remarkable progress has been achieved in the development of InGaN-based opto-electronic devices [17–21] the fundamental emission mechanism of InGaN, i.e. localization in local potential minima [22–25] versus piezoelectric fields [26], still remains a point of controversial discussion. In our measurements we directly evidence the alloy fluctuations in thick InGaN layers (i.e. no quantum wells), resulting in localized electronic states with different localization energies.

AlGaN is an essential component of GaN-based electronic devices [27] as well as for opto-electronic devices operating in the UV region [28, 29]. For efficient performance, high crystalline quality and chemical homogeneity of the AlGaN is mandatory. However, the mismatch of the lattice constants and the thermal expansion coefficients between AlGaN and potential substrates as well as GaN results in high densities of structural defects and in particular in micro-cracks [30–33]. Furthermore, the ternary alloy AlGaN is susceptible to fluctuations of the aluminum content, leading to laterally inhomogeneous strain and bandgap. In this paper, [Al]-fluctuations and local strain distributions in AlGaN layers are quantitatively evaluated. Growth of AlGaN on patterned substrates [34] is demonstrated to be accompanied by the self-organized formation of microscopic and nanoscopic domains with specific aluminum content [10].

Cathodoluminescence (CL) microscopy [35, 36] has proven its immense potential to characterize the evolution of the epitaxial lateral overgrowth of GaN (ELOG) on stripe masks, evidencing the formation of specific growth domains with typical properties for a variety of mask patterns and growth conditions [37–42]. In these investigations, 2D imaging was performed either on cleaved faces perpendicular to the c-plane or on the as-grown sample surface [43]. While this method is fully appropriate for ELOG on stripe masks, it only gives incomplete information for grid-like mask patterns. One approach to perform 3D characterization is to consecutively remove the ELOG layer to clearly defined depths [44, 45]. Here we present such a full 3D characterization of columnar ELOG domains formed during overgrowth of hexagonal masks [46].

The most significant measure for light-emitting diodes (LEDs) eventually fabricated from the nitrides is their electroluminescence (EL) since it probes the relevant properties of the fully processed device under operation [47]. The spectrally and spatially resolved micro-EL and SNOM-EL allow a direct microscopic correlation of the morphological and optical properties of the device.

## 2 Experimental techniques

Scanning cathodoluminescence (CL) microscopy provides a powerful tool comprising low and variable temperatures, high spatial resolution  $\Delta x < 45$  nm and high spectral resolution. In cathodoluminescence the sample under investigation is excited by the highly focused electron beam of a Scanning Electron Microscope (SEM). Our CL-system combines low temperatures ( $5\text{ K} < T < 300\text{ K}$ ), an overall spatial resolution of  $\Delta x < 45$  nm (under optimum conditions) with high spectral resolution. However, the unique feature of our CL system is the imaging of complete CL spectra [35], [36]. While the focused e-beam is digitally scanned over typically  $256 \times 200$  pixels a complete CL spectrum  $I(\lambda)_{x,y}$  is recorded at each pixel  $(x,y)$  and stored. A four-dimensional data set  $I_{CL}(x,y,\lambda)$  is obtained and consecutively evaluated. All type of data cross sections through this  $I_{CL}(x,y,\lambda)$  tensor can be generated, e.g. sets of monochromatic CL images  $I_{CL}(x,y,\lambda_1)$ ,  $I_{CL}(x,y,\lambda_2), \dots$ ; local CL spot spectra  $I_{CL}(x_1,y_1,\lambda)$ ,  $I_{CL}(x_2,y_2,\lambda)$ , ...; CL spectrum line scans  $I_{CL}(s,\lambda)$  ( $s$  = arbitrary line scan); as well as CL wavelength images (CLWI)  $\lambda_{max}(x,y)$ , i.e. mappings of the local CL emission peak wavelength  $\lambda_{max}$  [35, 48].

Our EL measurements are performed using a scanning micro-photoluminescence setup ( $\mu$ -PL) [49] as well as a combined scanning near field optical microscope (SNOM) / scanning electron microscope (SEM) system. The scanning  $\mu$ -PL /  $\mu$ -EL setup [47] is based on an optical microscope using long distance lenses transparent to UV. Here, the sample itself is scanned using computer controlled scanning

stages. A DC-motor driven stage enables the scanning with a resolution of 250 nm, piezo scanners are used for higher resolution. When operating in EL-mode, the  $\mu$ -EL is measured spatially resolved through the microscope in detection mode with an overall spatial resolution of 1  $\mu\text{m}$ . The luminescence is dispersed by a 0.5 m spectrometer with a spectral resolution of 0.5 nm and detected by a liquid nitrogen cooled UV-sensitive Si-CCD camera. The  $\mu$ -EL measurements reported here were all performed at room temperature. Our unique combined SNOM / SEM setup enables SNOM-EL, SNOM-PL, as well as cathodoluminescence and SEM imaging at the same sample position. The EL is collected via a fiber tip of an atomic force microscope mounted inside a SEM cathodoluminescence setup. The EL is dispersed by a 0.3 m spectrometer, and detected by liquid cooled CCD camera. The data recording procedure for scanning-EL-microscopy is directly adapted from our CL imaging technique. During a single scan over the area of interest a complete EL spectrum is recorded at each pixel and stored together with the morphology image obtained from AFM mode. As for our CL measurements, also for both EL-microscopy techniques described above, all types of data cross sections through the 4-dimensional EL data set  $I_{EL}(x,y,\lambda)$  are subsequently generated, such as local EL spot spectra, sets of mono-chromatic EL images, as well as EL wavelength images (ELWI), i.e. mappings of the local EL emission peak wavelength  $\lambda_{max}(x,y)$ .

Micro-Raman-spectroscopy ( $\mu$ -Raman) measurements were carried out in backscattering geometry at variable temperature. With the 488 nm line of an Ar<sup>+</sup>/Kr<sup>+</sup> gas laser for excitation, frequencies of the Raman signal can be determined with an accuracy of 0.1  $\text{cm}^{-1}$ . The lateral spatial resolution is 0.7  $\mu\text{m}$  [50].

### 3 Compositional fluctuations in thick InGaN layers

To establish the nanoscopic correlation of In-fluctuation with local luminescence spectra, CL microscopy was directly performed on the sample slices prepared for transmission electron microscopy (TEM). The sample was grown in a standard MBE system on a (0001) orientated sapphire substrate, utilizing a radio frequency plasma source for the supply of nitrogen. Details are given elsewhere [51]. The structure consists of 950 nm  $\text{In}_x\text{Ga}_{1-x}\text{N}$  deposited on a 30 nm GaN epilayer. The average indium content is  $x = 0.08$  as determined from high-resolution X-ray diffraction (HRXRD).

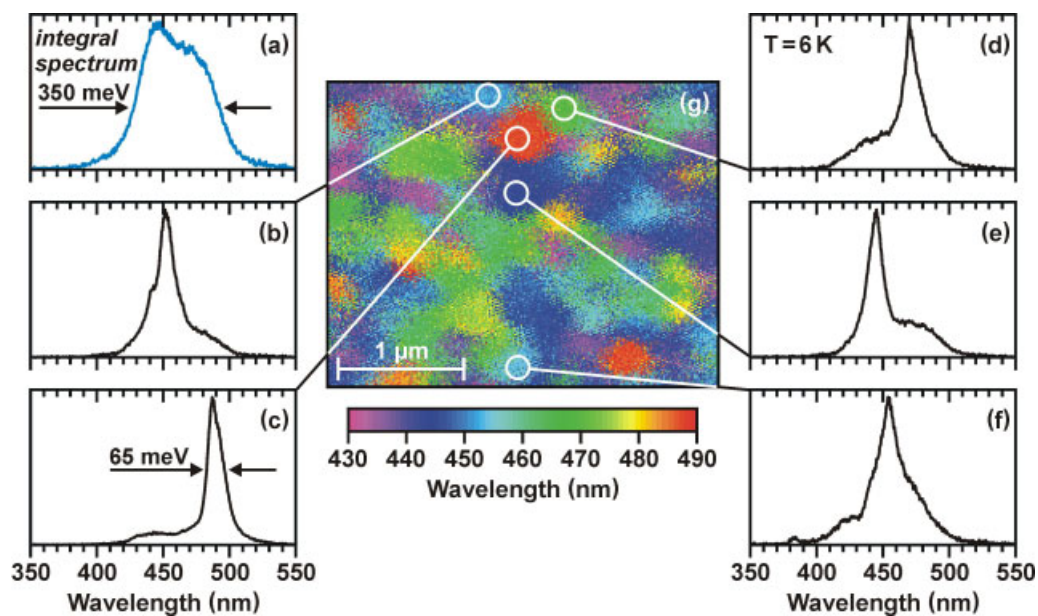


**Fig. 1** (online colour at [www.interscience.wiley.com](http://www.interscience.wiley.com)) Compositional fluctuations in a  $\sim 1 \mu\text{m}$  thick InGaN layer: a) laterally averaged CL spectrum of the sample surface and visualization of the local bandgap by b)-f) local CL spectra and g) a CL wavelength image.

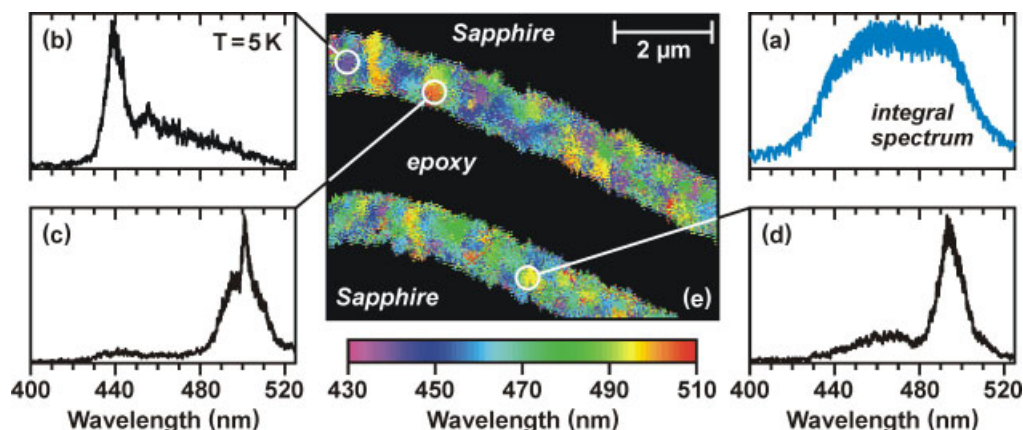


**Fig. 2** (online colour at [www.interscience.wiley.com](http://www.interscience.wiley.com)) Compositional fluctuations along the cross-section of a  $\sim 1 \mu\text{m}$  thick InGaN layer: a) laterally averaged CL spectrum of a specimen prepared for TEM investigations, b)-d) local CL spectra as well as e) CL wavelength image.

The integral CL spectrum of the sample, spatially averaged over  $3 \mu\text{m} \times 2 \mu\text{m}$ , is depicted in Fig. 1(a). A broad emission line centered at about 460 nm with a full width at half maximum (FWHM) of 350 meV is obtained which is also found in spatially integrating photoluminescence spectroscopy. However, a strong lateral fluctuation of the local CL peak wavelength is observed in CL scans, directly visualizing the fluctuations of indium content. Small areas with strongly differing but constant emission wavelength, i.e. specific [In], are clearly visible in the CLWI Fig. 1(g). Local spot-mode CL spectra recorded from the regions indicated in the CLWI are shown in Fig. 1(b)–(f).

As clearly seen, the FWHM of the individual peaks in the local spectra is considerably reduced with respect to the averaged spectrum Fig. 1(a). The size of the areas with constant emission wavelength varies between 50 nm and 500 nm, corresponding to the individual size of the potential minimum.

In principle, capture into the domains of lower energy may deteriorate the spatial resolution. However, in the CLWI (Fig. 1(g)) the average size of the regions of red shifted CL is barely larger than those of the blue shifted CL. As this diffusion and relaxation processes only occur from islands of larger energy to those of lower energy, resulting in a virtual larger size of the red islands and a virtual smaller size of the blue islands, these effects are negligible and the CLWI in Fig. 1(g) visualizes the true microscopic lateral Indium fluctuation.

A further increase of spatial resolution is achieved using an extremely thinned specimen as prepared for TEM. In addition to top-view scans of the as-grown sample surface, cross-sectional CL investigations were performed on the TEM specimens, which were prepared by mechanical grinding to about  $5 \mu\text{m}$  thickness followed by xenon ion milling at 5 kV down to electron transparency. Figure 2(e) shows a corresponding cross-sectional CLWI including two pieces of the sample glued face to face. A drift, caused by a gradual charging of the epoxy and sapphire substrate during scanning, is superimposed to the image.

The FWHM of the laterally averaged spectrum Fig. 2(a) compares to the results of the plan-view scans Fig. 1(a). Again, local spectra give rise to much narrower lines, e.g. in Fig. 2(c), demonstrating the improvement of spatial resolution. Additionally, areas of low emission energy can be seen to reach throughout the whole InGaN layer, evidencing the formation of columnar structures of local In-accumulation. These CL results are in perfect agreement with the TEM and TEM-EDX measurements on this specimen [51].

#### 4 Analysis of thick crack-free Aluminum-rich AlGaIn layers

The  $\text{Al}_x\text{Ga}_{1-x}\text{N}$  layers were grown by MOVPE on sapphire substrates. Prior to  $\text{Al}_x\text{Ga}_{1-x}\text{N}$  growth,  $2 \mu\text{m}$  GaN were deposited on a 30 nm low-temperature AlN buffer (LT-AlN, [52, 53]), covered again by LT-AlN. The three samples presented here have an average Aluminum molar fraction of  $x = 0.44$ ,  $x = 0.61$ ,

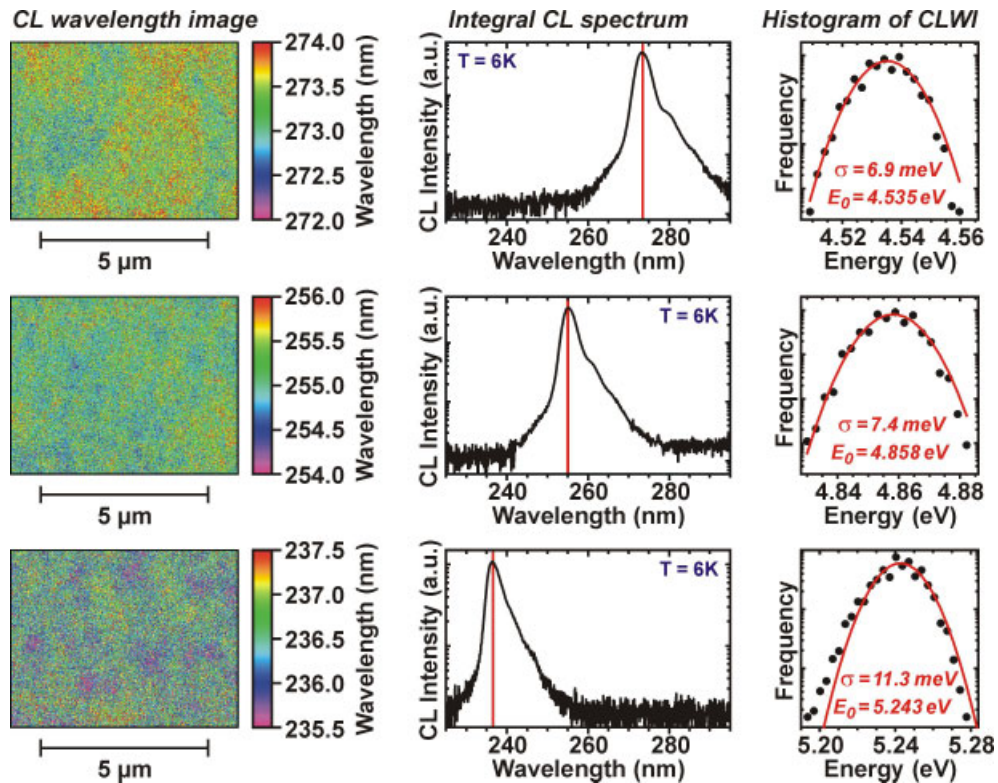


**Fig. 3** (online colour at [www.interscience.wiley.com](http://www.interscience.wiley.com)) Compositional fluctuations in AlGaIn layers with  $x = 0.44, 0.61$ , and  $0.76$  (top to bottom): CL wavelength images, laterally integrated CL spectra, as well as histograms of the CLWIs.

and  $x = 0.76$ , respectively [54]. Micro-cracks, which often accompany the growth of AlGaIn with high aluminum content [30], are completely absent in these  $\text{Al}_x\text{Ga}_{1-x}\text{In}$  layers even at  $x = 0.76$ .

The high-energy excitation sources of choice for optical investigations of these samples are either excimer lasers in PL or the electron beam excitation in CL.

In both laterally integrating PL and CL investigations an intense emission of the AlGaIn layers is detected, which shows a monotonous dependence on the nominal aluminum content  $x$ . As displayed in the laterally integrated CL spectra in Fig. 3, the AlGaIn peak position shifts from  $\lambda = 273$  nm for  $x = 0.44$  to  $\lambda = 255$  nm for  $x = 0.61$ , and finally to  $\lambda = 236$  nm for  $x = 0.76$ , in perfect agreement with the PL results [54].

The statistical fluctuations of the local Al incorporation were evaluated by CL wavelength mapping. The left hand column of Fig. 3 shows CL wavelength images taken at  $T = 6$  K. These images qualitatively visualize the extremely low fluctuations of the CL peak position, i.e. the local bandgap. The quantitative analysis of the CLWIs yields the histograms shown in the right hand column of Fig. 3, proving a narrow and perfect random distribution of the peak maximum positions given by a Gaussian function for all samples. No deviation from the purely statistical fluctuation of a perfect random alloy due to local clustering or even large phase separations is observed. The sharpness of the Gaussians evidences the good homogeneity of the ternary alloys. Even at  $x = 0.76$  the standard deviation of the peak position of  $E_0 = 5.243$  eV is as low as  $\sigma = 11.3$  meV over an area of  $6 \mu\text{m} \times 4 \mu\text{m}$ , as derived from the histogram of the CLWI in the bottom right corner in Fig. 3.

## 5 Stress relaxation at micro-cracks in AlGaIn

The sample under investigation is a  $0.56 \mu\text{m}$  thick  $\text{Al}_{0.17}\text{Ga}_{0.83}\text{In}$  epilayer grown by metal organic vapor phase epitaxy (MOVPE) on a  $1.9 \mu\text{m}$  thick GaN buffer on top of a sapphire substrate. The Al content



was determined by X-ray diffraction (XRD) taking into account the strain state [30]. Micro-cracks forming a hexagonal (trigonal) network are observed in the epilayer.

On this  $\text{Al}_{0.17}\text{Ga}_{0.83}\text{N}$  epilayer depth resolved CL spectroscopy was performed. A depth dependence of the CL signal was obtained by varying the penetration range  $R_e$  which is given by the voltage  $V_{\text{Beam}}$  accelerating the electron beam inside the SEM. In our experiments, the accelerating voltage  $V_{\text{Beam}}$  was varied from 3 kV to 20 kV, corresponding to a maximum penetration depth in a range between 0.1 and 2.2  $\mu\text{m}$ , as calculated from the Kanaya-Okayama model [55].

CLWIs corresponding to different accelerating voltages  $V_{\text{Beam}}$  (i.e. different depths) but the identical sampling position are shown in the left hand column of Fig. 4. The CLWIs exhibit a blue shift of the main emission line from the crack-free areas towards the actual position of the micro-cracks, as also observed elsewhere for cracked AlGaIn layers [56], [31]. This blue shift directly visualizes the lateral relaxation of the biaxial tensile stress in the AlGaIn layer at the cracks.

In vertical direction, i.e. corresponding to different acceleration voltages, the maximum shift of the CL emission wavelength increases from the AlGaIn/GaN interface towards the AlGaIn surface.

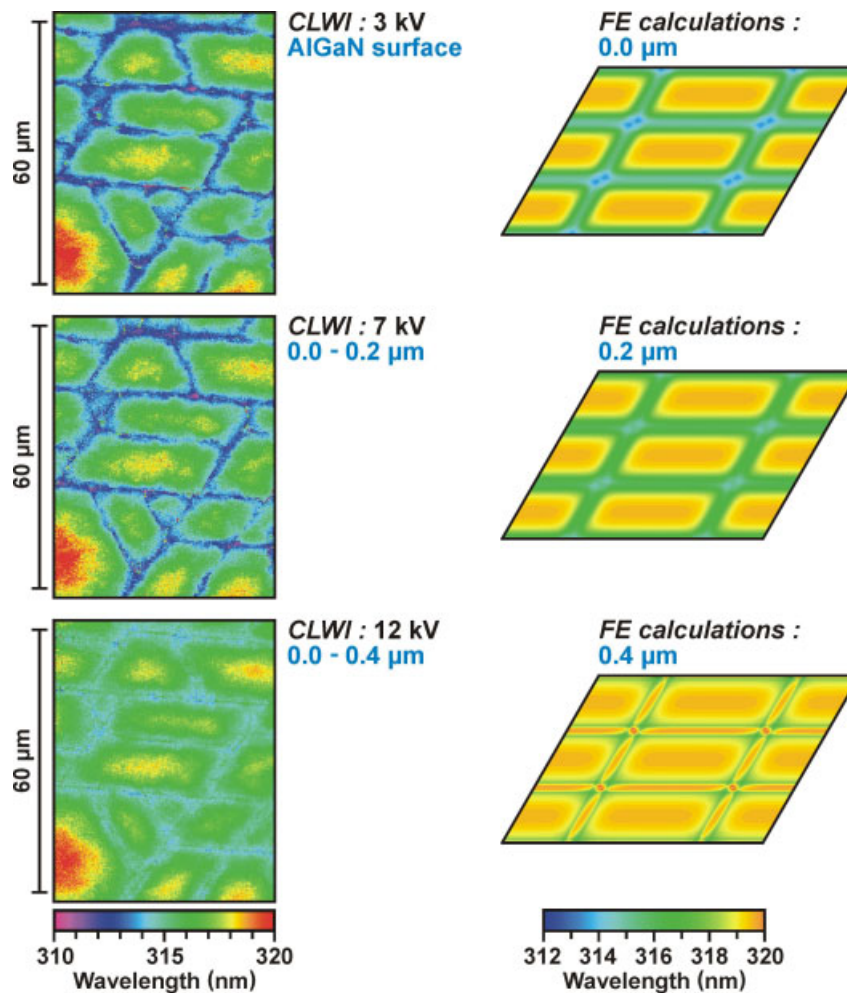


**Fig. 4** (online colour at [www.interscience.wiley.com](http://www.interscience.wiley.com)) Local relaxation of tensile stress in AlGaIn due to the formation of micro-cracks: CL wavelength images corresponding to different penetration ranges of the electron beam as well as calculations of the emission wavelength derived from a 3D theoretical analysis of the stress distribution by the finite-element method.

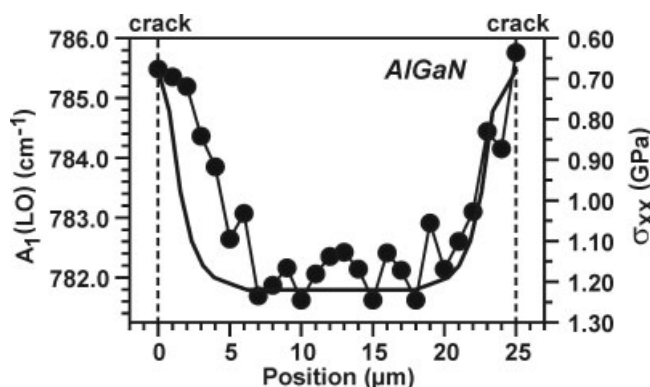


**Fig. 5** Evolution of stress between two cracks in the AlGaIn layer: Comparison between the experimental stress profile calculated from  $\mu$ -Raman using the  $A_1(\text{LO})$  phonon line (dots) and the theoretical prediction derived from a finite-element analysis (line).

The shift of the local CL emission wavelength directly correlates with the theoretical stress distribution between the cracks calculated from elasticity theory using a 3-dimensional finite-element (FE) approach [57–59]. Details are given elsewhere [60]. As the most frequent and recognizable pattern in the micro-crack network is the parallelogram, such a periodic crack arrangement was used during modeling. The right hand column of Fig. 4 shows the theoretical stress distribution already converted in the distribution of the local band gap, i.e. the local emission wavelength.

At the surface a monotonous decrease of tensile stress towards the cracks, i.e. a monotonous blue shift, is found. This blue shift reaches its maximum at the very crack position, as experimentally observed by CL.

In contrast to the surface case, a stress relaxation towards the cracks followed by a subsequent increase of the tensile stress in the direct vicinity of the cracks is calculated near the AlGaIn/GaN interface. Thus, near the cracks a local red shift of the emission wavelength is expected with increasing the maximum penetration depth. In the strained regions far away from the cracks only weak stress dependence is found both in the FE calculations and the CL measurements.

The overall consistent description of the stress distributions by CL microscopy and FE simulation is confirmed by micro-Raman spectroscopy. Due to the spectral overlap of the  $E_2$  mode of the AlGaIn layer and the  $E_2$  mode of the GaN buffer, the  $A_1(\text{LO})$  mode of AlGaIn was used to derive the stress distribution, although it is not optimal for the estimation of the stress due to the polar character. As evidenced by Fig. 5, the AlGaIn layer is tensile strained between the cracks and continuously relaxes towards the crack position.

## 6 Lateral seeding epitaxy of AlGaIn on trench patterned GaN

For GaN, a strong reduction of dislocation density is possible by applying masking techniques, e.g. epitaxial lateral overgrowth (ELOG) [61, 62] or pendeo epitaxy. However, these methods are not appropriate for AlGaIn because the Al-alloys also nucleate on the mask materials [1, 63]. Recently, growth on substrates periodically patterned into terraces and trenches has been proven successful to achieve thick, crack-free AlGaIn layers [34, 64, 65],[66]. However this method is liable to the formation of specific micro-domains in the thick AlGaIn layers, exhibiting different Al-concentrations [10, 11], as will be directly visualized by cross-sectional scanning CL microscopy in the following (Fig. 6).

The crack-free, 5  $\mu\text{m}$  thick AlGaIn layer ( $[\text{Al}] = 0.19$ ) was deposited by MOVPE growth on patterned GaN/LT-AlN/Sapphire substrates. Prior to the final AlGaIn growth, a periodic grid of trenches along  $\langle 1\bar{1}00 \rangle$  (5  $\mu\text{m}$  wide / 1  $\mu\text{m}$  deep) was fabricated in the 4  $\mu\text{m}$  GaN layer and subsequently overgrown with a LT-AlN interlayer [52, 53] as schematically illustrated in Fig. 6(c).

Three distinctly separated spectral components **A**, **B**, and **C** appearing in the laterally integrated CL spectra Fig. 6(b) can be unambiguously assigned to three different species of micro-domains.



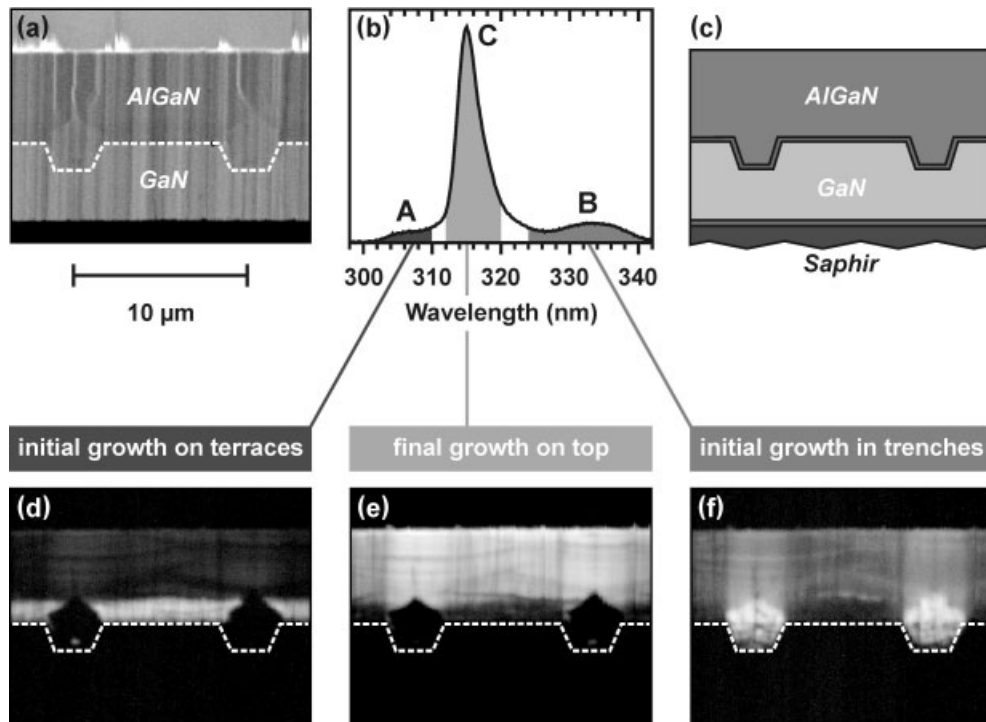


**Fig. 6** Self-organized micro-domains with different emission energy, i.e. specific aluminum content, in AlGaIn grown on a patterned GaN/Sapphire substrate: a) cross-sectional SEM image, b) CL spectrum averaged over the area of the SEM image, c) schematic sample setup as well as d)-f) CL intensity images in the spectral ranges indicated in b). The profile of the patterned GaN layer is given by the dotted line.

In Fig. 6, the region of initial AlGaIn growth on the terraces emits high-energetic luminescence centered at 305 nm (**A**). As seen in Fig. 6(d), with advancing vertical growth this domain also expands laterally over the trenches, finally leading to coalescence above the trench centers. In strong contrast, the domain of initial AlGaIn growth inside the trenches is completely dominated by low-energetic luminescence near 335 nm (**B**), indicating a strong Ga accumulation. This domain **B** gives rise to the bright areas in the intensity image Fig. 6(f). The lateral size of this domain **B** is limited by the trench width. The self-organized lateral expansion of **A** eventually inhibits further vertical growth of **B**, leading to the pentagonal shape in the cross-section Fig. 6(f).

While **A** and **B** clearly reflect the template patterning, the emission wavelength of the final domain **C** is almost independent of the lateral sampling position. Following the self-organized transition from domains **A** and **B** to **C**, we find an average emission wavelength of 315 nm (**C**) up to the sample surface. Thus, domain **C** laterally extends over the whole area of the sample as indicated in Fig. 6(e).

Using  $\mu$ -Raman to directly determine the local [Al], we find a perfect agreement with the CL results. Here, the Al-concentration is calculated from the  $A_1(\text{TO})$  phonon energy [67], [68], [69], [70].

In Fig. 7 we compare  $\mu$ -Raman line scans along  $\langle 0001 \rangle$  for two different lateral positions. The line scan Fig. 7(a) crosses the trench center. Above the GaN layer, it initially shows an aluminum concentration of [Al] = 0.09 inside the trenches, exactly where an emission wavelength of 335 nm is measured by CL inside **B**. Following the abrupt transition to **C**, above the trenches we find [Al] = 0.17 consistent with the CL emission wavelength near 315 nm. In comparison, the  $\mu$ -Raman line scan Fig. 7(b) runs through the terrace center. It proves [Al] = 0.22 directly above the terraces, where CL gives an emission wavelength of 305 nm inside **A**. Underneath the sample surface [Al] = 0.17 is reached, i.e. the identical value as for the upper region above the terraces in (a).

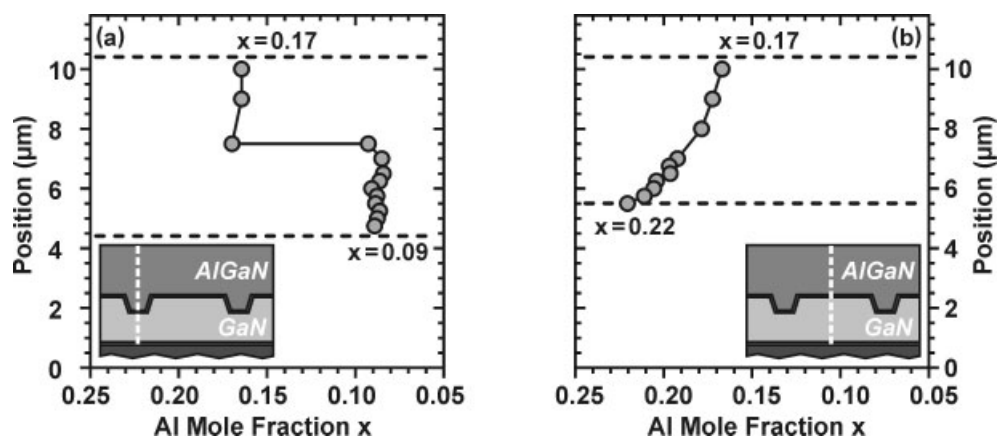


Fig. 7 Evolution of Aluminum content as derived from  $\mu$ -Raman using the  $A_1(\text{TO})$  position: a) line scan along the  $c$ -axis running through the terrace center, and b) line scan crossing the terrace center.

All three types of micro-domains **A**, **B**, and **C** additionally show specific nanoscopic modulations of their average Al-concentration. For a complete 3D visualization of these complex domain structures, cleavage planes of different crystallographic orientation were prepared and subsequently investigated by CL.

The upper row of Fig. 8 schematically indicates the CL scan direction used for the CLWIs in the lower row of Fig. 8. This way, Fig. 8(a) shows a scan parallel to  $\{1\bar{1}20\}$ , where the cleavage plane runs along the trench center. For Fig. 8(c), the sample was cleaved along  $\{1\bar{1}20\}$ . In contrast to (a), the cleavage plane now follows the terrace center. Fig. 8(b) shows a cleaved face parallel to  $\{1\bar{1}00\}$ , i.e. perpendicular to the trench direction.

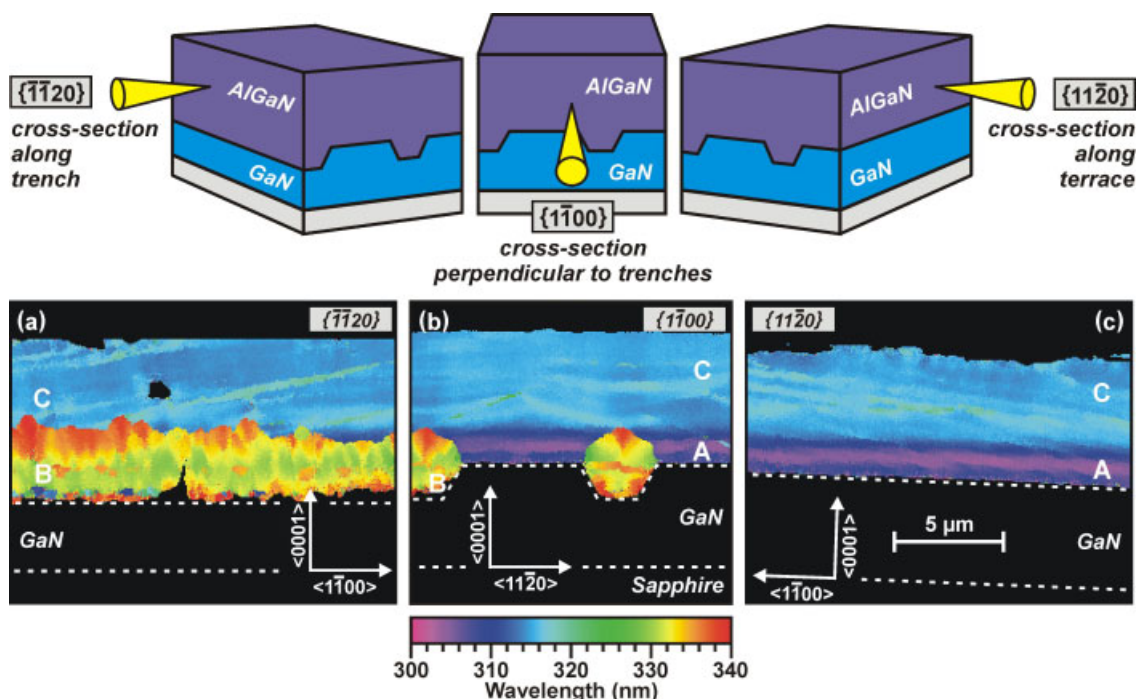


Fig. 8 (online colour at [www.interscience.wiley.com](http://www.interscience.wiley.com)) Three-dimensional characterization of the nanoscopic [Al]-modulations by CL wavelength imaging on differently oriented cross-sections: a) parallel to  $\{1\bar{1}20\}$  in trench, b) parallel to  $\{1\bar{1}00\}$  as well as c) parallel to  $\{1\bar{1}20\}$  on terrace.

In **A** we observe an initial overall blue shift of the peak position compensated by a comparable red shift, indicating a vertical gradient of aluminum content.

In **B** we find statistical fluctuations of the peak position, i.e. the local Al-concentration, for the very first growth stage at the trench bottom. AlGa<sub>N</sub> growth on the trench side facets is initially accompanied by emission red shifted up to 340 nm. All domains **B** exhibit a strong red shift of the emission wavelength from the outer trench edges towards the domain top, indicating a gradual Ga-accumulation during growth.

Domain **C** exhibits strong vertical modulations of the average emission energy, appearing as curved lines of red shifted luminescence, i.e. increased [Ga], in Fig. 8(b). The cross-sectional CLWIs parallel to  $\{11\bar{2}0\}$  reveal the real three-dimensional, marble-like geometry of these modulations. In Fig. 8(a) and (c), these [Al]-modulations inside **C** are visualized by tilted, parallel lines of red shifted luminescence, running straight to the sample surface.

Sporadic Ga-rich defects in the otherwise homogeneous surface emission energy, as visible in the plan-view CLWI of the as-grown (0001) sample surface Fig. 9(b), appear exactly where these planes of the marbled structure penetrate the sample surface. This effect is illustrated by the CLWIs Fig. 9(a) and Fig. 9(c), both showing cross-sectional and surface emission of domain **C** at once.

The positions of these Ga-rich defects always coincide with nanoscopic steps on the planar AlGa<sub>N</sub> surface. The existence of these steps may give an explanation of the marble-like structure in **C**. As proposed by [71], preferential incorporation of Ga at the step sites caused by the different surface mobility of Ga and Al could lead to a local Ga accumulation. Thus, a lateral movement of the step positions during vertical expansion of the AlGa<sub>N</sub> layer leaves behind traces of tilted Ga-rich planes, as clearly observed inside domain **C**.

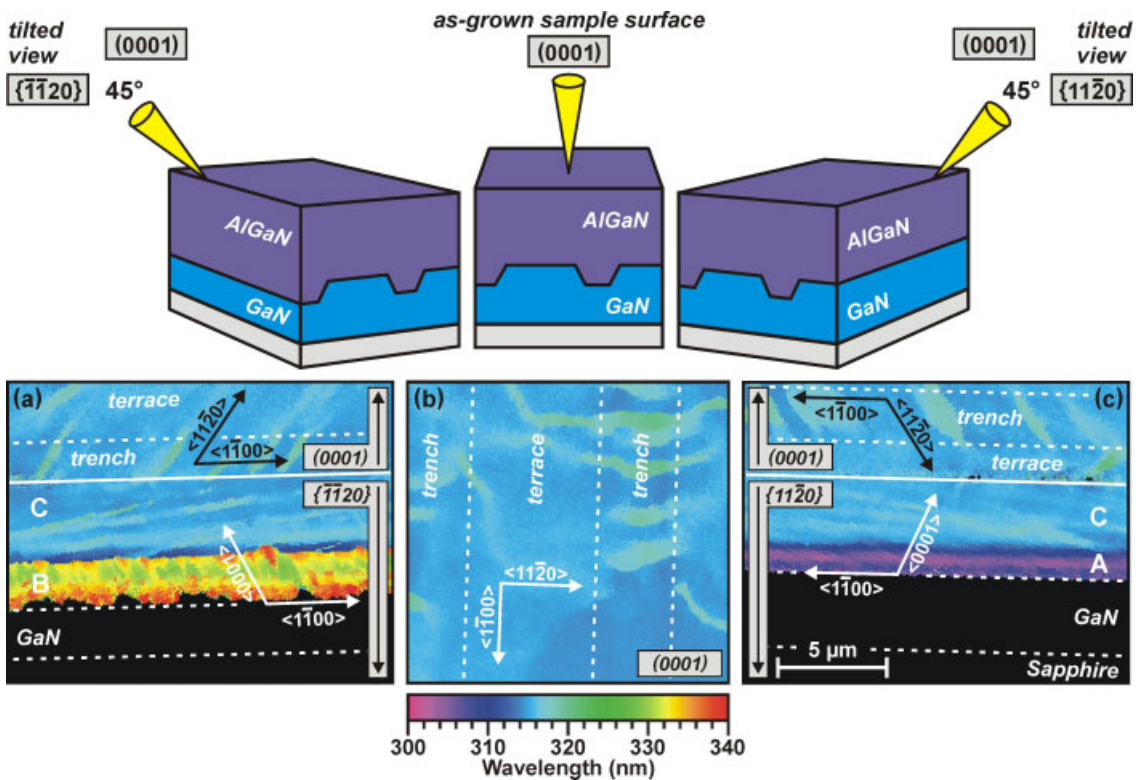


**Fig. 9** (online colour at [www.interscience.wiley.com](http://www.interscience.wiley.com)) Marble-like [Al]-modulations in the domain of final AlGa<sub>N</sub> growth visualized by CL wavelength imaging: a) tilted view of the transition from  $\{11\bar{2}0\}$  in trench to surface, b) plan-view image of the as-grown sample surface as well as c) tilted view of the transition from  $\{11\bar{2}0\}$  on terrace to surface.

## 7 Formation of growth domains in ELOG on hexagonal mask patterns

As comprehensively evidenced in our previous studies [5, 6, 7, 38], the selective growth of GaN, especially the epitaxial lateral overgrowth of GaN (ELOG) is always accompanied by the self-organized evolution of characteristic growth domains. The specific optical and electronic properties of the individual domains, e.g. caused by specific impurity incorporation, have been shown to directly correlate with the facet structure of the GaN surface during selective growth [36, 40, 41].

While the complete characterization of the domain properties on stripe mask patterns is usually achieved by cross-sectional CL investigations perpendicular to the mask direction, grid-like patterns are experimentally more challenging. Here we present the characterization of columnar growth domains formed in a thick GaN layer during lateral overgrowth of hexagonal masks [46].

The sample growth started with the deposition of a 2  $\mu\text{m}$  MOVPE GaN buffer on (0001) sapphire substrate. On top of the GaN buffer, a SiO<sub>2</sub>-layer was patterned by photolithography and wet chemical etching into a periodic mask of 7  $\mu\text{m}$  wide SiO<sub>2</sub>-hexagons set 11  $\mu\text{m}$  apart. Subsequently, these patterned templates were overgrown in an AIXTRON horizontal HVPE system.

In conjunction with our 'standard' cross-sectional CL imaging at cleaved faces perpendicular to the *c*-plane (Fig. 10), a direct visualization of the 3D domain formation in the HVPE layer was achieved by consecutive vertical series of mappings parallel to the *c*-plane (Fig. 11). For these depth-resolved CL investigations a 2.4 mm wide spherical pit was fabricated in the ELO-GaN by mechanical grinding and polishing, reaching through the MOVPE buffer layer at its very center. The pit profile was determined using a surface profiler, establishing the correlation between depth and lateral position. CL maps were

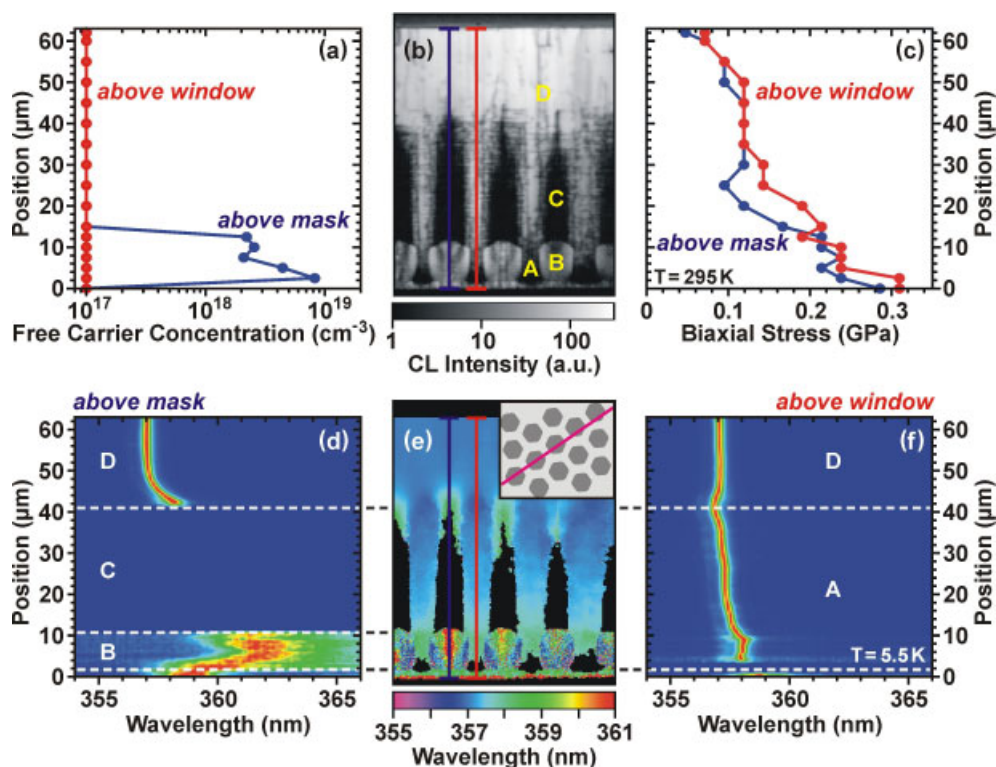


**Fig. 10** (online colour at [www.interscience.wiley.com](http://www.interscience.wiley.com)) Columnar growth domains in ELOG on hexagonal mask patterns: a) evolution of local free carrier concentration along the *c*-axis, b) cross-sectional CL intensity image, c) evolution of stress along the *c*-axis, d) and f) evolution of near band edge emission along the *c*-axis, as well as e) CL wavelength image of the identical area depicted in b).



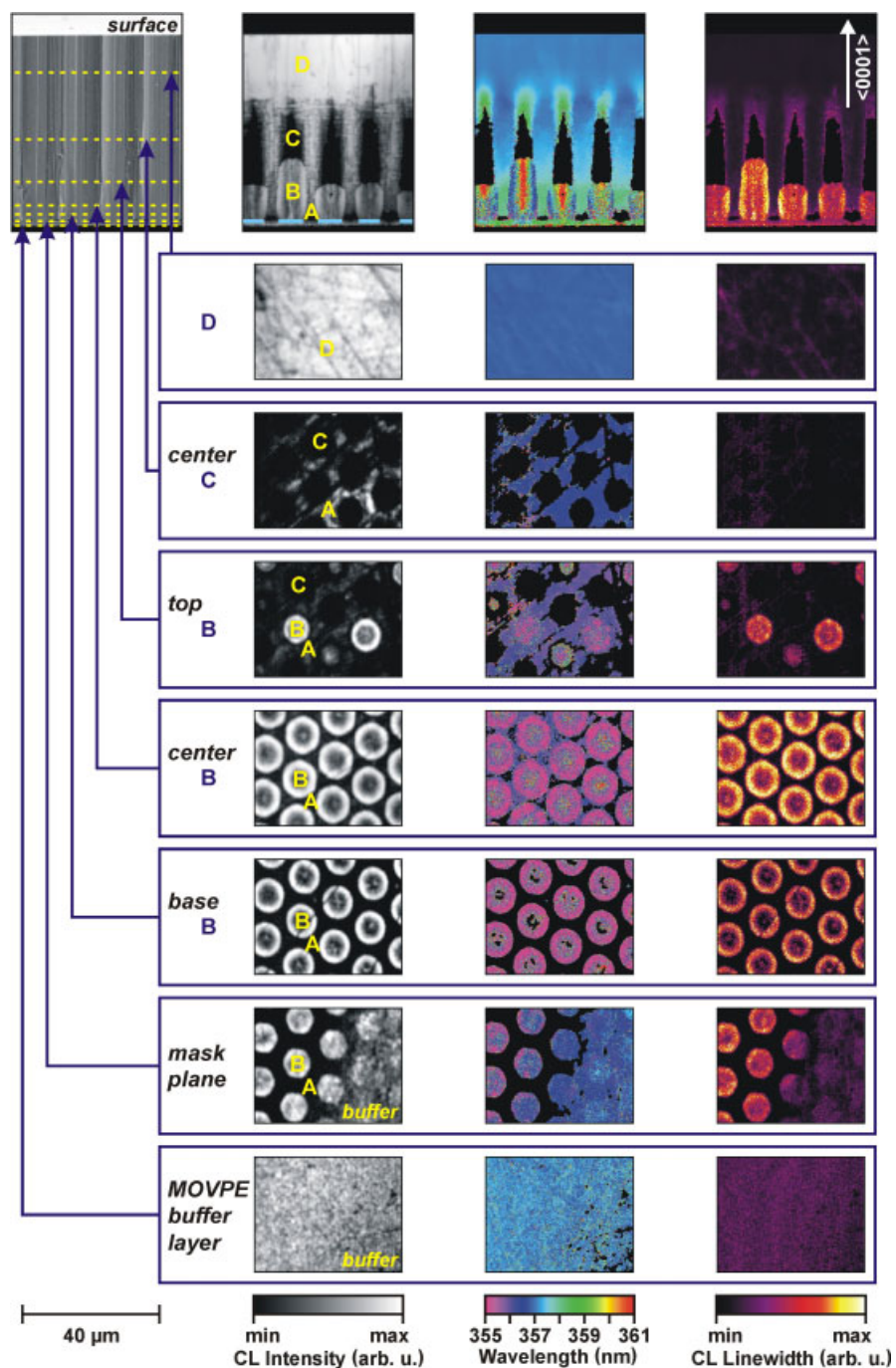


**Fig. 11** (online colour at [www.interscience.wiley.com](http://www.interscience.wiley.com)) Three-dimensional characterization of columnar growth domains in ELOG on hexagonal mask patterns: upper row: cross-sectional SEM image perpendicular to the *c*-plane, CL intensity image, CLWI and CL line width map of the identical sampling position; below: series of cross-sectional maps parallel to the *c*-plane at different depths.

taken at different lateral positions with respect to the pit center, leading to a series of cross-sectional images almost parallel to the *c*-plane but at increasing *c*-position ranging from the buffer layer up to the ELOG surface. For 50  $\mu\text{m}$  wide maps used here, the spherical inclination of the pit slopes results in a depth difference, which is well below 1  $\mu\text{m}$  (1.1 deg.) in the mask plane and about 5  $\mu\text{m}$  (5.7 deg.) directly underneath the sample surface.

Figures 10(b) and (e) show cross-sectional mappings of the ELOG layer perpendicular to the *c*-plane. While at the left-hand side of these images the cleaved face almost crosses the centers of the hexagonal masks, at the right-hand side only the mask edges are met. This is illustrated by the magenta line in the schematic mask pattern depicted in the inset of Fig. 10(e).

A variety of distinct features showing characteristic luminescence properties are visible in the integral CL intensity image (CLI) of the near band edge emission Fig. 10(b), and the CL wavelength image (CLWI) Fig. 10(e), both displaying the identical area. These features directly correspond to specific growth domains formed during the evolution of the ELO GaN, marked in Fig. 10(b).

Initial (0001) growth in the unmasked areas (**A**) is characterized by sharp, however, weak excitonic emission, indicating a low impurity incorporation but high density of non-radiative recombination centers near the MOVPE / HVPE GaN interface. Directly underneath the mask-openings even the luminescence of the buffer is affected, showing an abrupt drop of quantum efficiency. With advancing (0001) growth the excitonic emission intensity above the unmasked areas gradually increases. A high density of dark lines running parallel to the horizontal mask plane is visible in the CL intensity image Fig 10(b) in this area. These lines of low quantum efficiency directly visualize dislocations bent perpendicular to the growth direction. The onset of faceted overgrowth (**B**) at the mask edges coincides with a drastic increase of integral CL intensity. This high integral intensity is exclusively caused by the appearance of broad and blue shifted (e,h)-plasma luminescence, as illustrated in Fig. 10(d). The indication of a high local free carrier concentration *n* inside **B**, as given by the (e,h)-emission, is confirmed by the  $\mu$ -Raman line scan Fig. 10(a), as will be discussed below.

The following lateral expansion of the ELO GaN towards the mask centers is accompanied by a gradual red shift of the plasma edge, i.e. a monotonous decrease of *n*.

In the coalescence region directly above the mask centers we preferentially find strongly red shifted extrinsic luminescence, which is consistent with strong impurity incorporation.

While the (0001) growth in **A** uninhibitedly extends up to the sample surface, the characteristic properties of **B** are restricted to self-limited columns with an average height of 10  $\mu\text{m}$ . Following a totally self-organized transition, further growth above the masks leads to an abrupt drop of the near band edge CL in 30  $\mu\text{m}$  high cone-shaped domains **C** (Fig 10(b)). Exactly here we preferentially find Yellow Luminescence indicating strong local incorporation of deep defect centers. In the final domain of 15  $\mu\text{m}$  (0001)-growth above and between the masks (**D**), no influence of the actual mask positions on the bright excitonic emission is found by CL, evidencing a homogeneous high quality of this upper layer.

Using the  $\mu$ -Raman line scans to directly determine *n*, we find a perfect agreement between the optical and electrical properties. In Fig. 10, CL line scans parallel to the *c*-axis in (d) and (f) (red contrast = high CL intensity) are compared with the corresponding evolution of *n* in (a). The CL line scan Fig. 10(f), running through a mask opening, is always dominated by the sharp excitonic emission found in **A** and **D**. A spectral blue shift of the excitonic line position along the *c*-axis is consistent with CL results on thick GaN layers [72], [73], [74]. In Fig. 10(a) the corresponding *n* never exceeds the detection limit of  $10^{17} \text{ cm}^{-3}$ . In total contrast, we observe an extremely high *n* reaching  $10^{19} \text{ cm}^{-3}$  directly above the masks, exactly where the CL line scan Fig. 10(d) exhibits the broad luminescence band inside **B**. Where the broad CL vanishes at the transition to **C**, *n* abruptly drops below the detection limit. Region **D** is characterized by sharp excitonic emission and a low *n* also above the masks.

In these cross-sectional investigations the shape of the columnar ELOG domains **A**, **B** and **C** depends on the actual orientation of the cleaved face. A complete 3D image is obtained by additional depth-resolved mappings parallel to the *c*-plane. In Fig. 11 a consecutive series of such CLI and CLWI mappings is displayed. The vertical sampling positions of these mappings are indicated in the cross-sectional SEM image in the upper row of Fig. 11. For each cross-section the lateral distribution of the CL intensity, local emission wavelength and CL line width are depicted in one row.



In the lowest row the series shows the granular structure of the MOVPE GaN buffer. The high defect density of the buffer layer is illustrated by a high density of dark spots visualizing the drop of quantum efficiency around dislocations. In the next row the mask plane is met. Due to the slight inclination of the spherical pit surface both the upper part of the buffer and the onset of the HVPE growth are visible. Directly above the MOVPE / HVPE interface, the grid-like pattern of **A** interchanges with the hexagonal shapes of **B**. In the following cross-sections, the high integral CL intensity, blue shifted and broad emission of the (e,h)-plasma luminescence inside **B** is clearly visualized in ring-like structures appearing in the CLI, CLWI and line width map, respectively. Above, at some mask positions the very tops of **B** are still seen, while at other mask positions the transition to **C** has already occurred.

Following the cross-section running through the center of **C**, the homogeneity of **D** is evidenced in the uppermost row of the series. A network of defects appearing in the images corresponds to scratches left from the mechanical treatment of the sample.

## 8 Microscopic LED device characterization

Scanning electroluminescence microscopy ( $\mu$ -EL) provides a fast and non-destructive method to analyze the homogeneity of a light-emitting device in its final, completely processed form. It yields a direct image of the spatial and spectral emission characteristics revealing imperfections of epitaxial growth as well as inhomogeneities of contact design and current injection [47, 75].

The light emitting diode (LED) under  $\mu$ -EL investigation is a commercially available InGaN/GaN single quantum well (SQW) LED of Nichia [76]. The active region of this LED consists of a 2 nm  $\text{In}_{0.2}\text{Ga}_{0.8}\text{N}$  SQW embedded in 100 nm  $\text{Al}_{0.3}\text{Ga}_{0.7}\text{N}$  and 50 nm  $\text{In}_{0.02}\text{Ga}_{0.98}\text{N}$  p- and n-type barriers. The lateral structure of the device is visible in the top-view optical microscope image in Fig. 12(d), showing the position of the p- and n-contacts.

The  $\mu$ -EL measurements were performed at room temperature using DC injection currents ranging from 0.2 mA up to 60 mA [77].

At 0.2 mA the homogeneous distribution of the EL intensity in Fig. 12(a) proves a laterally uniform current injection over the whole mesa. However, the spot-like appearance of the intensity distribution shows that the radiative recombination is restricted to strongly localized areas. In contrast, at higher injection current a homogeneous distribution of the EL intensity is found on a micro-scale. Nevertheless, at 60 mA the injected current is not longer homogeneously spread over the whole mesa, leading to a drop

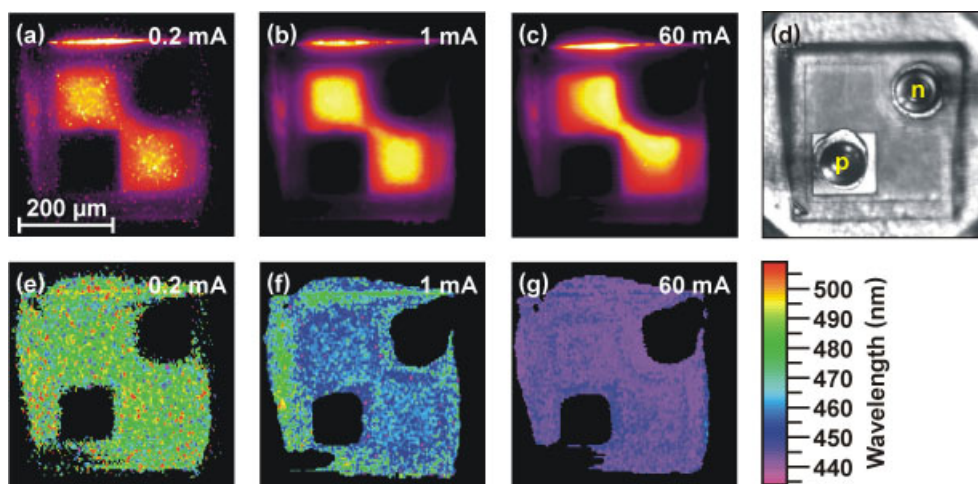


**Fig. 12** (online colour at [www.interscience.wiley.com](http://www.interscience.wiley.com)) Micro-electroluminescence maps of the commercial Nichia-LED under different injection currents: a)–c) spectrally integrating  $\mu$ -EL intensity images, each normalized to the maximum intensity, d) optical microscopy image, as well as e)–g) EL wavelength images.

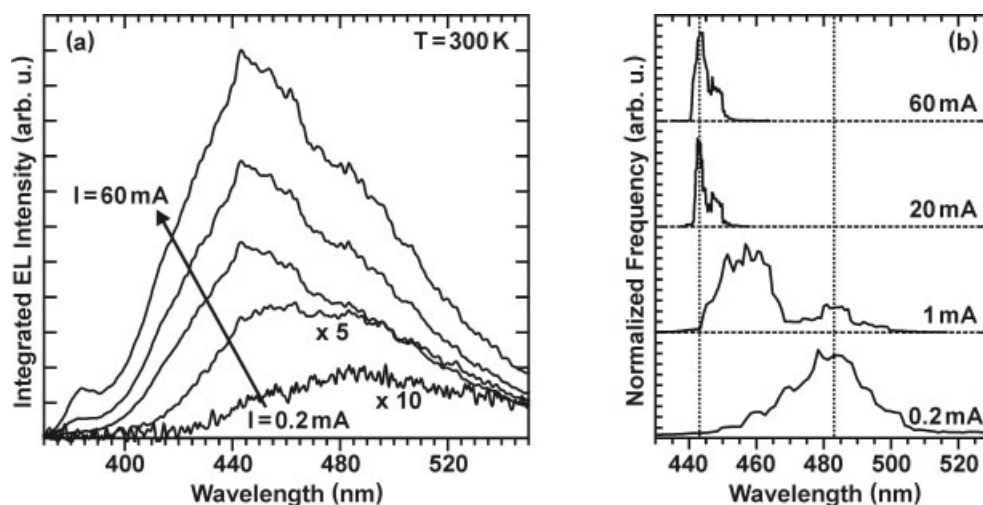


**Fig. 13** Spectral blue shift of the emission wavelength with increasing injection current for the commercial Nichia-LED: a) laterally integrated EL spectra, b) histograms of ELWIs (normalized to the maximum frequency and shifted with respect to each other).

of EL intensity from the n-type towards the p-type contact directly visualizing the onset of problems with hole injection at high currents.

The ELWIs Fig. 12(e)–(g) show a drastic overall blue shift of the emission energy with increasing injection current, which is explained by a fundamental transition between the dominant recombination channels.

At a low injection current of 0.2 mA the ELWI Fig. 12(e) shows an emission wavelength around 480 nm. Lateral fluctuations of the emission wavelength are associated with potential fluctuations in the InGaN SQW, exhibiting different localization energies. At low currents, the radiative recombination predominantly takes place after thermalization into these localized states, which are only partly filled. The blue shift of the emission wavelength with increasing injection current is assigned to a consecutive filling of the local potential minima. Above 20 mA the EL emission wavelength remains constant around 445 nm, proving the complete saturation of localized low-energy states.

Parallel to the spectral blue shift the emission wavelength shows a strong narrowing of its statistical distribution, as quantitatively expressed by the histograms Fig. 13(b). A competing recombination channel appearing at high currents around 380 nm in the EL spectra Fig. 13(a) is attributed to the  $\text{In}_{0.02}\text{Ga}_{0.98}\text{N}$  barrier indicating filling of the  $\text{In}_{0.2}\text{Ga}_{0.8}\text{N}$  SQW states under strong injection ( $I > 60$  mA).

## 9 Nano-characterization of LEDs: Origin of EL blue shift

In order to gain deeper insight into the microscopic mechanism of the light emission process and the nature of the blue shift always observed with increasing current, we need much higher spatial resolution reaching the nanometer scale. As an example for EL device characterization in our SNOM-EL system, we present blue InGaN/GaN multiple quantum well light emitting diodes under room temperature operation, which were grown on Silicon (111) substrate by MOVPE. Details of the fabrication of these bright blue LEDs on Si are given elsewhere [21].

The SNOM-ELWI in the center of Fig. 14 reveals local emission peak wavelengths between 450 nm and 550 nm. These lateral fluctuations of the EL energy directly image the nanoscopic fluctuations of the stoichiometry in the active InGaN-QWs of the device. The local EL spectra in Fig. 14 exhibit different center positions and intensities, and are superimposed by Fabry-Perot-interferences. The spectral positions of the interference maxima were found to be exactly identical over a wide area, proving a mirror-like surface and constant thickness of the whole diode stack.

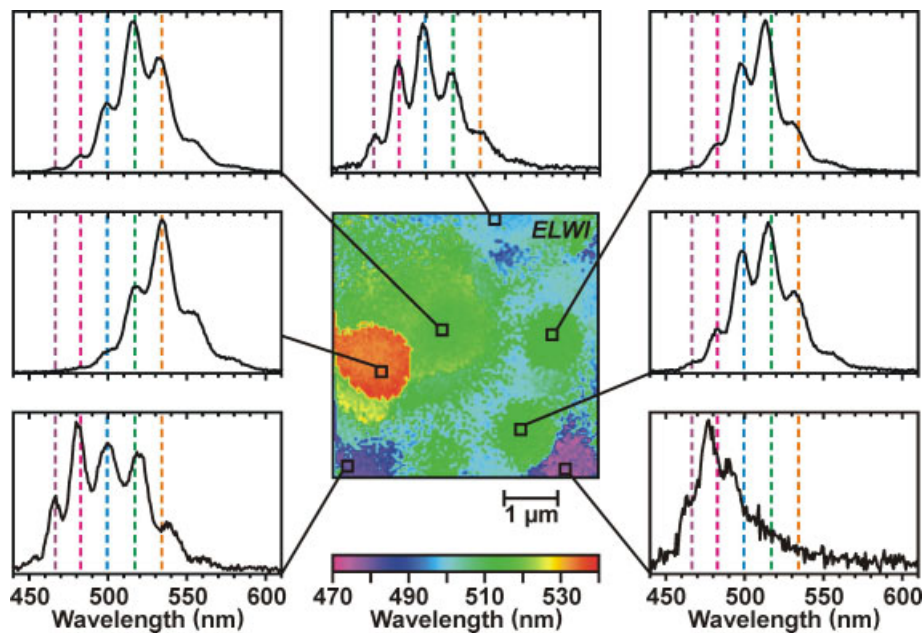


**Fig. 14** (online colour at [www.interscience.wiley.com](http://www.interscience.wiley.com)) Electro-Luminescence Wavelength Image (ELWI) and local EL spectra of an InGaN/GaN-LED under operation, taken in SNOM detection mode.

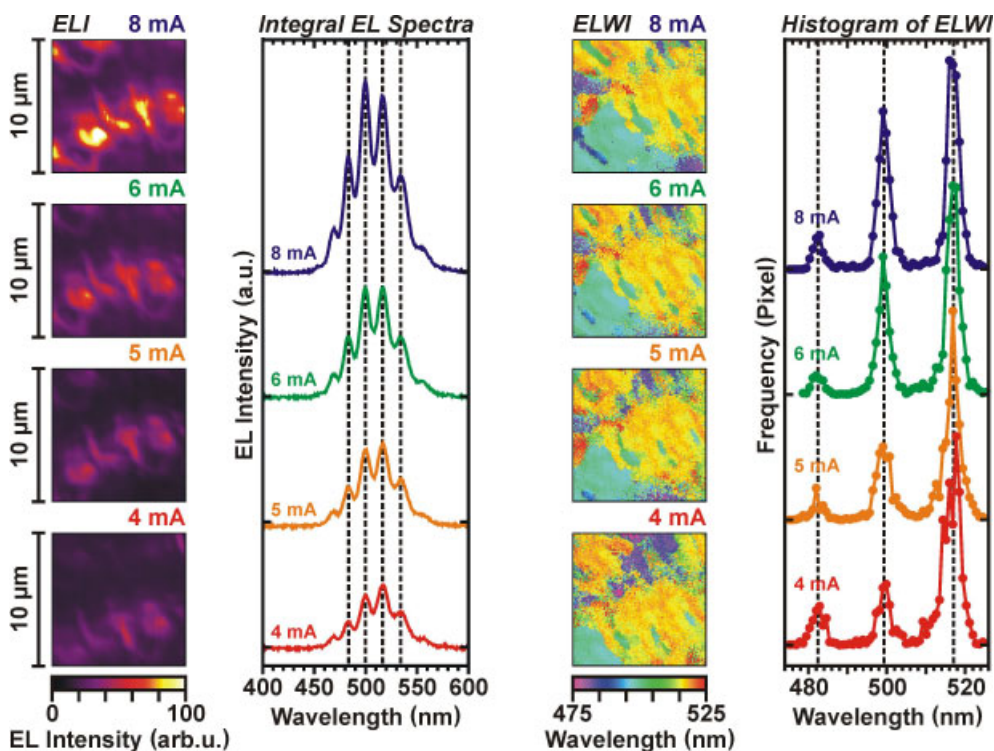


**Fig. 15** (online colour at [www.interscience.wiley.com](http://www.interscience.wiley.com)) Electroluminescence intensity images and ELWIs of an InGaN/GaN-LED under different injection currents, taken in the SNOM detection mode.

To understand the nanoscopic nature of the blue shift of EL with increasing current, the SNOM-EL-characterization was performed as a function of injection current. Figure 15 shows EL intensity images (ELIs), i.e. mappings of the spectrally integrated EL intensity (1. column from the left) and corresponding ELWIs of the identical sampling positions (3. column) as a function of increasing injection currents, ranging from  $I = 4$  mA to  $I = 8$  mA. The integral EL spectra, laterally integrated over the whole area of the ELIs, are depicted in the second column and the histograms of the ELWIs are given in the fourth column of Fig. 15.

A spot like pattern is clearly visible in the ELIs (all four plotted with identical intensity scale) proving that the EL emission only originates from nano-spots under these low injection conditions. The rising light output is accompanied by a spectral blue shift of the total EL, which is clearly visible in the integral EL spectra. This is visualized by the growing lateral size of the 498 nm wavelength domains (blue green contrast) with respect to the decreasing size of the 517 nm domains (yellow contrast) in the ELWIs.

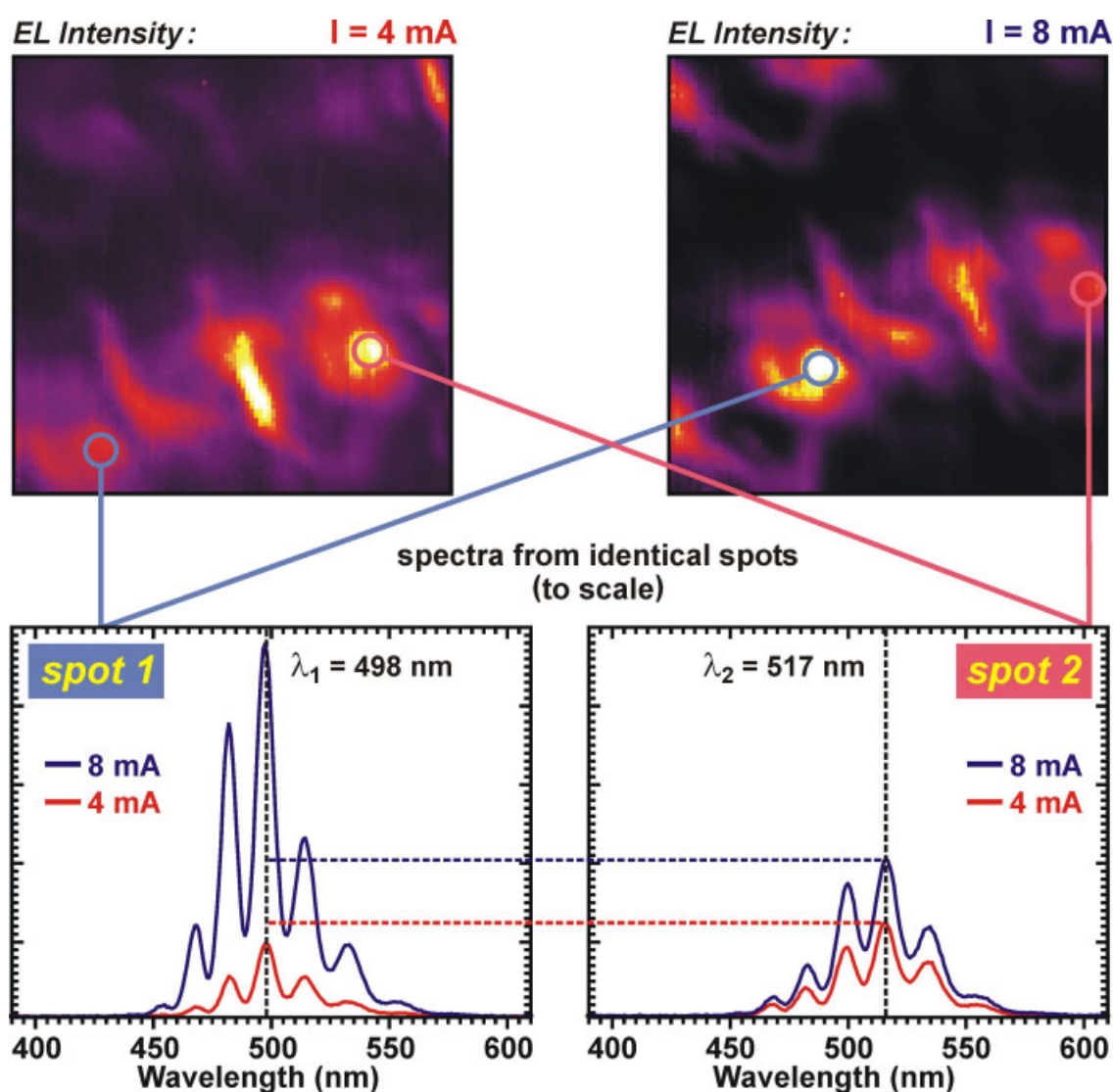


**Fig. 16** (online colour at [www.interscience.wiley.com](http://www.interscience.wiley.com)) SNOM-EL intensity images (relative scale) and local EL spectra (absolute scale) for injection currents of 4 mA and 8 mA visualizing the growing contribution of high-energy emission due to the saturation of the EL from low-energy potential minima.

The SNOM-EL measurements prove a gradual saturation of the originally dominating emission from low-energy local potential minima with increasing injection current. Thus, in the SNOM-EL maps the lateral size of the short wavelength domains increases, i.e. the blue green regions in the ELWIs in Fig. 15 gain size which is quantitatively expressed by the ELWI histograms in Fig. 15 evidencing the growing contribution of the Fabry-Perot-mode at 498 nm in comparison to that at 517 nm.

Let us now look more detailed into the underlying physics. The two ELI maps of Fig. 15 recorded for 4 mA and for 8 mA injection current are compared in Fig. 16, and two distinct different sub- $\mu\text{m}$  spots are identified in both ELIs. The relative intensity contrast is scaled separately to min/max for each ELI.

At 4 mA, the blue spot 1 is weaker in relative intensity than the red spot 2. In contrast, for 8 mA the situation is vice versa and the red spot 2 is relatively weaker than the blue spot 1. The nano-scale local spot spectra for spot 1 and spot 2 are depicted for 4 mA and for 8 mA in the lower row of Fig. 16.

Here the intensity scale is identical for all four spectra, which thus can be compared in absolute intensity. It is quite obvious that for both injection currents the emission peak at 498 nm dominates spot 1, while the EL at 517 nm always dominates spot 2. However, at 4 mA spot 2 is brighter in *absolute* intensity than spot 1, which gains much stronger in intensity on the current increase. For  $I = 8$  mA the ratio of the absolute intensities is inverted and spot 1 becomes dominant. As a result, with higher injection current the short wavelength emitting local micro spots take over in absolute EL intensity as compared to the long wavelength emitting micro spots. This microscopic effect results in an increasing contribution of short wavelength emission to the integral EL and eventually in the macroscopic observed shift of the integral EL spectrum to shorter wavelength.

## 10 Conclusions

Fluctuations of the indium content in a thick InGaN epilayer are directly imaged by highly spatially resolved CL microscopy. While the spatial resolution of plan-view investigations is still limited by the penetration range of the incident electron beam, a considerable improvement of resolution is evidenced in the TEM-CL mode. Columns of high [In] are found to reach throughout the whole thickness of the 1  $\mu\text{m}$  MBE-InGaN layer.

Extremely low fluctuations of the [Al]-dependent local bandgap are mapped and quantitatively analyzed for crack-free  $\text{Al}_x\text{Ga}_{1-x}\text{N}$  layers with  $x$  up to 0.76.

Combining cathodoluminescence and micro-Raman spectroscopy results with theoretical calculations, a comprehensive analysis of cracked  $\text{Al}_x\text{Ga}_{1-x}\text{N}$  epilayers is achieved. Here, the shift of the local near band-gap emission line of the AlGaIn layer follows the measured and calculated strain profile between the cracks.

AlGaIn grown on patterned GaN/Sapphire templates is found to be susceptible to the self-organized formation of Ga-rich AlGaIn micro domains, leading to a complex three-dimensional modulation of the optical and structural properties. During initial AlGaIn overgrowth of the template (patterned into terraces and trenches), the modulation of the local AlGaIn stoichiometry results in periodic structures of Ga accumulation clearly reflecting the pattern periodicity. Following planarization, a homogeneous emission wavelength, i.e. homogeneous aluminum content, is found near the sample surface. All AlGaIn micro-domains additionally show nanoscopic modulations of their specific aluminum content.

Columnar ELOG domains formed during HVPE overgrowth of hexagonal  $\text{SiO}_2$ -masks were 3D imaged by CL microscopy. The areas of initial (0001) growth between the masks show sharp excitonic luminescence and a local free carrier concentration  $n$  well below  $10^{17} \text{ cm}^{-3}$ . The first stage of faceted lateral overgrowth leads to 10  $\mu\text{m}$  high self-limited columns exhibiting broad (e,h)-plasma CL above the mask edges, extrinsic luminescence in the coalescence areas, and  $n$  reaching  $10^{19} \text{ cm}^{-3}$ . Subsequent growth above the masks results in an abrupt drop of  $n$  below  $10^{17} \text{ cm}^{-3}$  inside 30  $\mu\text{m}$  high cones emitting Yellow CL. The final ELOG domain (uppermost 15  $\mu\text{m}$ ) is completely dominated by excitonic CL above and between the masks, indicating a homogeneous high crystal quality at the sample surface.

As evidenced by SNOM investigations in the detection mode, the overall blue shift of the laterally averaged EL spectrum of the LED is a result of the microscopic fluctuations in local EL emission wavelength due to composition fluctuations and their competition in quantum efficiency as a function of carrier injection density.



**Acknowledgements** The authors thank the groups of D. Hommel (University of Bremen, Germany), H. Amano and I. Akasaki (Meijo University, Nagoya, Japan), K. J. Ebeling (University of Ulm, Germany), and A. Krost (Otto-von-Guericke University Magdeburg, Germany) for supplying the excellent samples. The authors are obliged to Q. K. K. Liu (Hahn-Meitner-Institute, Berlin, Germany) for contributing the finite-element calculations. We are indebted to T. Hempel (Otto-von-Guericke-University Magdeburg, Germany) for the SNOM investigations and to M. Zacharias (Otto-von-Guericke-University Magdeburg, Germany) for help with the  $\mu$ -EL measurements. The authors gratefully acknowledge financial support by the Deutsche Forschungsgemeinschaft (DFG) in the framework of contracts Nos. CH 87/4-1, CH 87/4-2, THO 662/4-1, and THO 662/4-2.

## References

- [1] Y. Kato, S. Kitamura, K. Hiramatsu, and N. Sawaki, *J. Cryst. Growth* **144**, 133 (1994).
- [2] A. Usui, H. Sunakawa, A. Sakai, and A. Yamaguchi, *Jpn. J. Appl. Phys.* **36**, L899 (1997).
- [3] P. Vennéguès, B. Beaumont, V. Bousquet, M. Vaille, and P. Gibart, *J. Appl. Phys.* **87**, 4175 (2000).
- [4] Y. Honda, Y. Iyechika, T. Maeda, H. Miyake, and K. Hiramatsu, *Jpn. J. Appl. Phys. Part 4A* **40**, L309 (2001).
- [5] F. Bertram, T. Riemann, J. Christen, A. Kaschner, A. Hoffmann, C. Thomsen, K. Hiramatsu, T. Shibata, and N. Sawaki, *Appl. Phys. Lett.* **74**, 359 (1999).
- [6] A. Kaschner, A. Hoffmann, C. Thomsen, F. Bertram, T. Riemann, J. Christen, K. Hiramatsu, T. Shibata, and N. Sawaki, *Appl. Phys. Lett.* **74**, 3320 (1999).
- [7] A. Kaschner, A. Hoffmann, C. Thomsen, F. Bertram, T. Riemann, J. Christen, K. Hiramatsu, H. Sone, and N. Sawaki, *Appl. Phys. Lett.* **76**, 3418 (2000).
- [8] J. W. P. Hsu, M. J. Matthews, D. Abusch-Magder, R. N. Kleiman, D. V. Lang, S. Richter, S. L. Gu, and T. F. Kuech, *Appl. Phys. Lett.* **79**, 761 (2001).
- [9] M. J. Matthews, J. W. P. Hsu, S. Gu, and T. F. Kuech, *Appl. Phys. Lett.* **79**, 3086 (2001).
- [10] T. Riemann, J. Christen, A. Kaschner, A. Laades, A. Hoffmann, C. Thomsen, M. Iwaya, S. Kamiyama, H. Amano, and I. Akasaki, *Appl. Phys. Lett.* **80**, 3093 (2002).
- [11] M. Iwaya, S. Terao, T. Sano, T. Ukai, R. Nakamura, S. Kamiyama, H. Amano, and I. Akasaki, *J. Cryst. Growth* **237-239**, 951 (2002).
- [12] S. Nakamura, M. Senoh, N. Iwasa, S. Nagahama, T. Yamada, and T. Mukai, *Jpn. J. Appl. Phys. Part 2* **10B**, L1332 (1995).
- [13] A. Dadgar, J. Christen, T. Riemann, S. Richter, J. Bläsing, A. Diez, A. Krost, A. Alam und M. Heuken, *Appl. Phys. Lett.* **78**, 2211 (2001).
- [14] I.-h. Ho and G. B. Stringfellow, *Appl. Phys. Lett.* **69**, 2701 (1996).
- [15] R. Singh, D. Doppalapudi, T. D. Moustakas, and L. T. Romano, *Appl. Phys. Lett.* **70**, 1089 (1997).
- [16] F. Bertram, S. Srinivasan, L. Geng, F. A. Ponce, T. Riemann, and J. Christen, *Appl. Phys. Lett.* **80**, 3524 (2002).
- [17] S. Nakamura, S. Senoh, N. Iwasa, and S. Nagahama, *Jpn. J. Appl. Phys. Part 2* **34**, L797 (1995).
- [18] S. Nakamura, M. Senoh, S. Nagahama, N. Iwasa, T. Yamada, T. Matsushita, H. Kiyoku, Y. Sugimoto, T. Kozaki, H. Umemoto, M. Sano, and K. Chocho, *Jpn. J. Appl. Phys. Part 2* **37**, L309 (1998).
- [19] A. Dadgar, A. Alam, T. Riemann, J. Bläsing, A. Diez, M. Poschenrieder, M. Straßburg, M. Heuken, J. Christen, and A. Krost, *phys. stat. sol. (a)* **188**, 155 (2001).
- [20] A. Dadgar, M. Poschenrieder, O. Contreras, J. Christen, K. Fehse, J. Bläsing, A. Diez, F. Schulze, T. Riemann, F. A. Ponce, and A. Krost, *phys. stat. sol. (a)* **192**, 308 (2002).
- [21] A. Dadgar, M. Poschenrieder, I. Daumiller, M. Kunze, A. Strittmatter, T. Riemann, F. Bertram, J. Bläsing, F. Schulze, A. Reiher, A. Krtischil, O. Contreras, A. Kaluza, A. Modlich, M. Kamp, L. Reißmann, A. Diez, J. Christen, F. A. Ponce, D. Bimberg, E. Kohn, and A. Krost, to appear in *phys. stat. sol. (c)* **0**, No. 5 (2003) (this volume).
- [22] S. Chichibu, T. Azuhata, T. Sota, and S. Nakamura, *Appl. Phys. Lett.* **70**, 2822 (1997).
- [23] S. Chichibu, K. Wada, and S. Nakamura, *Appl. Phys. Lett.* **71**, 2346 (1997).
- [24] Y. Narukawa, Y. Kawakami, M. Funato, S. Fujita, S. Fujita, and S. Nakamura, *Appl. Phys. Lett.* **70**, 981 (1997).
- [25] T. Riemann, D. Rudloff, J. Christen, A. Krost, M. Lünenbürger, H. Protzmann, and M. Heuken, *phys. stat. sol. (b)* **216**, 301 (1999).
- [26] H. Kollmer, J. S. Im, S. Heppel, J. Off, F. Scholz, and A. Hangleiter, *Appl. Phys. Lett.* **74**, 82 (1999).
- [27] M. Asif Khan, X. Hu, A. Tarakij, G. Simin, J. Yang, R. Gaska, and M. S. Shur, *Appl. Phys. Lett.* **77**, 1339 (2000).



- [28] S. Nakamura, M. Senoh, S. Nagahama, N. Iwasa, T. Yamada, T. Matsushita, Y. Sugimoto, and H. Kiyoku, *Appl. Phys. Lett.* **69**, 4056 (1996).
- [29] D. J. H. Lambert, M. M. Wong, U. Chowdhury, C. Collins, T. Li, H. K. Kwon, B. S. Shelton, T. G. Zhu, J. C. Campbell, and R. D. Dupuis, *Appl. Phys. Lett.* **77**, 1900 (2000).
- [30] S. Einfeldt, V. Kirchner, H. Heinke, M. Dießelberg, S. Figge, K. Vogeler, and D. Hommel, *J. Appl. Phys.* **88**, 7029 (2000).
- [31] D. Rudloff, T. Riemann, J. Christen, K. Vogeler, S. Einfeldt, D. Hommel, A. Kaschner, A. Hoffmann, and C. Thomsen, *Proc. Int. Workshop on Nitride Semicond., IPAP Conf. Ser.* **1**, 475 (2000).
- [32] M. Iwaya, S. Terao, N. Hayashi, T. Kashima, H. Amano, and I. Akasaki, *Appl. Surf. Sci.* **159-160**, 405 (2000).
- [33] S. Einfeldt, M. Dießelberg, H. Heinke, D. Hommel, D. Rudloff, J. Christen, and R. F. Davis, *J. Appl. Phys.* **92**, 118 (2002).
- [34] M. Iwaya, R. Nakamura, S. Terao, T. Ukai, S. Kamiyama, H. Amano, and I. Akasaki, *Proc. Int. Workshop Nitride Semiconductors (IWN2000), IPAP Conf. Series* **1**, 833 (2000).
- [35] J. Christen, M. Grundmann, and D. Bimberg, *J. Vac. Sci. Technol. B* **9**, 2358 (1991).
- [36] J. Christen and T. Riemann, *phys. stat. sol. (b)*, **419** (2001).
- [37] J. A. Freitas, Jr., O.-H. Nam, R. F. Davis, G. V. Saparin, and S. K. Obyden, *Appl. Phys. Lett.* **72**, 2990 (1998).
- [38] T. Riemann, J. Christen, A. Kaschner, A. Hoffmann, C. Thomsen, O. Parillaud, V. Wagner, and M. Ilegems, in: *Proc. of the IWN2000, IPAP Conf. Series* **1**, 475 (2000).
- [39] E. Feltin, B. Beaumont, P. Vennéguès, T. Riemann, J. Christen, J. P. Faurie, and P. Gibart, *phys. stat. sol. (a)* **188**, 733 (2001).
- [40] S. Gradecak, V. Wagner, M. Ilegems, T. Riemann, J. Christen, and P. Stadelmann, *Appl. Phys. Lett.* **80**, 2866 (2002).
- [41] V. Wagner, O. Parillaud, H. J. Bühlmann, M. Ilegems, S. Gradecak, P. Stadelmann, T. Riemann, and J. Christen, *J. Appl. Phys.* **92**, 1307 (2002).
- [42] H. Miyake, S. Bohyama, M. Fukui, K. Hiramatsu, Y. Iyechika, and T. Maeda, *J. Cryst. Growth* **237-239**, 1055 (2002).
- [43] S. J. Rosner, G. Girolami, H. Marchand, P. T. Fini, J. P. Ibbetson, L. Zhao, S. Keller, U. K. Mishra, S. P. Den-Baars, and J. S. Speck, *Appl. Phys. Lett.* **74**, 2035 (1999).
- [44] S. Dassonneville, A. Amokrane, B. Sieber, J. L. Farvacque, B. Beaumont, and P. Gibart, *J. Appl. Phys.* **89**, 3736 (2001).
- [45] S. Dassonneville, A. Amokrane, B. Sieber, J. L. Farvacque, B. Beaumont, G. Gibart, J.-D. Ganiere, and K. Leifer, *J. Appl. Phys.* **89**, 7966 (2001).
- [46] T. Riemann, J. Christen, A. Kaschner, A. Hoffmann, C. Thomsen, M. Seyboth, F. Habel, R. Beccard, and M. Heuken, *phys. stat. sol. (a)* **188**, 751 (2001).
- [47] P. Fischer, J. Christen, M. Zacharias, V. Schwegler, C. Kirchner, and M. Kamp, *phys. stat. sol. (a)* **176**, 119 (1999).
- [48] J. Christen, *Adv. Solid State Phys.* **30**, 239 (1990).
- [49] P. Fischer, J. Christen, M. Zacharias, H. Nakshima, and K. Hiramatsu, *Solid State Phenom.* **63**, 151 (1998).
- [50] H. Siegle, L. Eckey, A. Hoffmann, C. Thomsen, B. K. Meyer, D. Schikora, M. Hankeln, K. Lischka, *Solid State Commun.* **96**, 943 (1995).
- [51] H. Selke, M. Amirsawadkouhi, P. L. Ryder, T. Böttcher, S. Einfeldt, D. Hommel, F. Bertram, and J. Christen, *Mater. Sci. Eng. B* **59**, 279 (1999).
- [52] H. Amano, N. Sawaki, I. Akasaki, and Y. Toyoda, *Appl. Phys. Lett.* **48**, 353 (1986).
- [53] Y. Koide, N. Itoh, K. Itoh, N. Sawaki, and I. Akasaki, *Jpn. J. Appl. Phys.* **27**, 1156 (1988).
- [54] B. K. Meyer, G. Steude, A. Göldner, A. Hoffmann, H. Amano, and I. Akasaki, *phys. stat. sol. (b)* **216**, 187 (1999).
- [55] K. Kanaya and S. Okayama, *J. Phys. D: Appl. Phys.* **5**, 43 (1972).
- [56] L. H. Robins and D. K. Wickenden, *Appl. Phys. Lett.* **71**, 3841 (1997).
- [57] MARC, McNeal-Schwendler Corp, USA, User's Guide 2000.
- [58] Q. K. K. Liu, A. Hoffmann, H. Siegle, A. Kaschner, C. Thomsen, J. Christen, and F. Bertram, *Appl. Phys. Lett.* **74**, 3122 (1999).
- [59] Q. Liu, A. Hoffmann, A. Kaschner, C. Thomsen, J. Christen, P. Veit, and R. Clos, *Jpn. J. Appl. Phys. Part 2* **10A**, L958 (2000).
- [60] D. Rudloff, T. Riemann, J. Christen, Q. K. K. Liu, A. Kaschner, A. Hoffmann, C. Thomsen, M. Dießelberg, S. Einfeldt, and D. Hommel, to appear in *Appl. Phys. Lett.* **81**, (2002).
- [61] K. Hiramatsu, *J. Phys.: Condens. Matter* **13**, 6961 (2001).
- [62] B. Beaumont, Ph. Vennéguès, and P. Gibart, *phys. stat. sol. (b)* **227**, 1 (2001).

- [63] T. Detchprohm, S. Sano, S. Mochizuki, S. Kamiyama, H. Amano, and I. Akasaki, *phys. stat. sol. (a)* **188**, 799 (2001).
- [64] M. Yano, T. Detchprohm, R. Nakamura, S. Sano, S. Mochizuki, T. Nakamura, H. Amano, and I. Akasaki, *Proc. Int. Workshop Nitride Semiconductors (IWN2000)*, IPAP Conf. Series **1**, 292 (2000).
- [65] T. Detchprohm, M. Yano, S. Sano, R. Nakamura, S. Mochizuki, T. Nakamura, H. Amano, and I. Akasaki, *Jpn. J. Appl. Phys. Part 2* **40**, L16 (2001).
- [66] S. Mochizuki, T. Detchprohm, S. Sano, T. Nakamura, H. Amano, and I. Akasaki, *J. Cryst. Growth* **237-239**, 1065 (2002).
- [67] H. Siegle, Ph. D. thesis, Technical University Berlin, Germany (1998).
- [68] A. Cros, H. Angerer, O. Ambacher, M. Stutzmann, R. Höpler, and T. Metzger, *Solid State Commun.* **104**, 35 (1997).
- [69] L. Bergman, M. D. Bremser, W. G. Perry, R. F. Davis, M. Dutta, and R. J. Nernanich, *Appl. Phys. Lett.* **71**, 2157 (1997).
- [70] F. Demangeot, G. Groenen, J. Frandon, M. A. Renucci, O. Briot, S. Clur, and R. L. Aulornbard, *Appl. Phys. Lett.* **72**, 2674 (1998).
- [71] A. Petersson, A. Gustafsson, L. Samuelson, S. Tanaka, and Y. Aoyagi, *MRS Internet J. Nitride Semicond. Res.* **7**, 5 (2001).
- [72] H. Siegle, A. Hoffmann, L. Eckey, C. Thomsen, J. Christen, F. Bertram, M. Schmidt, D. Rudloff, and K. Hiramatsu, *Appl. Phys. Lett.* **71**, 2490 (1997).
- [73] F. Bertram, S. Srinivasan, F. A. Ponce, T. Riemann, J. Christen, and R. J. Molnar, *Appl. Phys. Lett.* **78**, 1222 (2001).
- [74] W. Zhang, T. Riemann, H. R. Alves, M. Heuken, D. Meister, W. Kriegseis, D. M. Hoffmann, J. Christen, A. Krost, and B. K. Meyer, *J. Cryst. Growth* **234**, 616 (2002).
- [75] P. Fischer, J. Christen, M. Zacharias, V. Schwegler, C. Kirchner, and M. Kamp, *Jpn. J. Appl. Phys. Part 1* **39**, 2414 (2000).
- [76] S. Nakamura, M. Senoh, N. Iwasa, and S. Nagahama, *Appl. Phys. Lett.* **67**, 13 (1995).
- [77] P. Fischer, J. Christen, and S. Nakamura, *Jpn. J. Appl. Phys. Part 2* **39**, L129 (2000).